Supplementary Information (SI) for Nanoscale.
This journal is © The Royal Society of Chemistry 2026

Supplementary information

Nanoscale thermocapillary flow as a recording medium for infrared absorption spectra of individual carbon nanotubes

Kai Watanabe[1], Shigeo Maruyama[1,2,3], Keigo Otsuka[1,*]

[1] Department of Mechanical Engineering, Faculty of Engineering, The University of Tokyo, Tokyo, 113-8656, Japan.

[2] School of Mechanical Engineering, Zhejiang University, Hangzhou, 310027, China.

[3] Institute of Innovation for Future Society, Nagoya University, Nagoya, 464-0861, Japan

*Email: otsuka@photon.t.u-tokyo.ac.jp

Methods

Detailed Simulation Conditions

The thermofluidic simulation framework was based on the model reported by Song et al. [1]. For given spatial profiles of shear stress and surface tension, the governing equation for thermocapillary flow is given by

$$\frac{\partial h}{\partial t} + \frac{\partial}{\partial x}\left[\frac{\tau h^2}{2\mu} + \frac{h^3}{3\mu}\frac{\partial}{\partial x}\left(\gamma \frac{\partial^2 h}{\partial x^2}\right)\right] = 0$$

where $h(x,t)$ is the film thickness, μ is the film viscosity, τ denotes the shear stress at the film surface induced by the surface-tension gradient, and $\gamma(x)$ is the surface tension. The thin film and substrate were represented in two dimensions using square cells with a side length of 2 nm. The substrate was assumed to be a 100 nm SiO_2 layer on silicon, and the thin film was assumed to be PMMA. The initial film thickness was set to 24 nm, and the substrate thickness was 100 nm. For a localized heat source at the origin cell with heat generation $P = Q\,dV$ where Q is a volumetric heat source and dV is the volume of a single cell, two-dimensional temperature distributions in the film and substrate were described by heat conduction equation

$$C_V \frac{\partial T}{\partial t} = \kappa\left(\frac{\partial^2}{\partial x^2} + \frac{\partial^2}{\partial y^2}\right)T + Q$$

by using their respective volumetric heat capacities (C_{film} and $C_{\text{substrate}}$) and thermal conductivities. In this model, CNT heat sources were assumed to be sufficiently separated so that thermal interference between adjacent CNTs could be neglected. Therefore, periodic boundary conditions were imposed along the *x*-direction. Furthermore, because the thermal conductivity of the quartz substrate is much higher than that of the PMMA film, the temperature rise in the substrate due to CNT heating was assumed to be negligible. Accordingly, a constant-temperature boundary condition was applied at the bottom of the 100 nm-thick substrate in the *y*-direction. In order to take the film deformation due to the thermocapillary flow into account, we introduced $\eta(x,y,t)$, defined as a continuous variable ranging from 0 to 1, representing the local volume fraction of the film within each cell. In the initial state, $\eta = 1$ in the region occupied by the film, and a 30 nm vacuum region with $\eta = 0$ was defined above the film. Heat conduction was allowed only in regions where $\eta \neq 0$. At the film surface, where cells with $\eta \neq 0$ were adjacent to vacuum cells ($\eta = 0$), heat transfer between the film and vacuum was neglected, and an adiabatic boundary condition was applied. The local film thickness $h(x,t)$ was defined as $h(x,t) = \int \eta(x,y,t)\,dy$.

The temperature dependence of the film viscosity $\mu(T)$ was described using the Williams–Landel–Ferry (WLF) equation,

$$\log\left(\frac{\mu(T)}{\mu(T_0)}\right) = -\frac{C_1(T-T_0)}{C_2+(T-T_0)}$$

The parameters were determined based on the data reported by Sidorov et al [2].

Table. 1 Parameters of WLF equation reported by Sidorov et al [2].

Parameter	PMMA
$\boldsymbol{\mu(T_0)}$, Pa · s	13450
$\boldsymbol{T_0}$, °C	200
$\boldsymbol{C_1}$	7.6682
$\boldsymbol{C_2}$, °C	210.76

Chirality assignment by Raman spectroscopy

The chirality assignment was performed based on Raman spectroscopy. The radial breathing mode (RBM) frequency measured under 532 nm excitation was used to estimate the CNT diameter. Possible candidate chiralities were then narrowed down using the Kataura plot in conjunction with the excitation energy. The electronic type (metallic or semiconducting) was further evaluated from the G-band line shape, which is known to exhibit characteristic features depending on the CNT electronic structure; semiconducting CNTs typically show a relatively narrow [3]. Based on the observed G-band line shape, the CNT was classified as semiconducting, which is consistent with the assignment of a (23,7) nanotube.

We note that the chirality assignment is not strictly unique, as nearby chiralities with similar diameters may also be consistent with the measured RBM frequency. Therefore, we discuss alternative candidate chiralities and the corresponding redshift in Fig. S5.

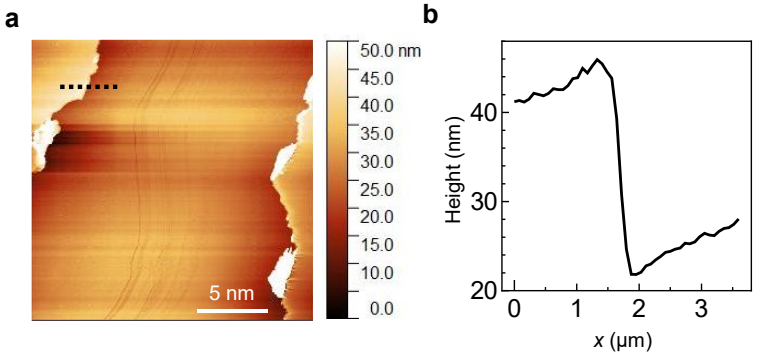

Fig. S1 (a) AFM image of the boundary between the region with the PMMA thin film and the region without the film. (b) Cross-sectional height profile taken along the dotted line indicated in (a).

The film thickness was determined by mechanically removing a portion of the PMMA layer from the spin-coated substrate using a metal probe and subsequently measuring a height profile by AFM. The thickness of the PMMA thin film was found to be 24 nm.

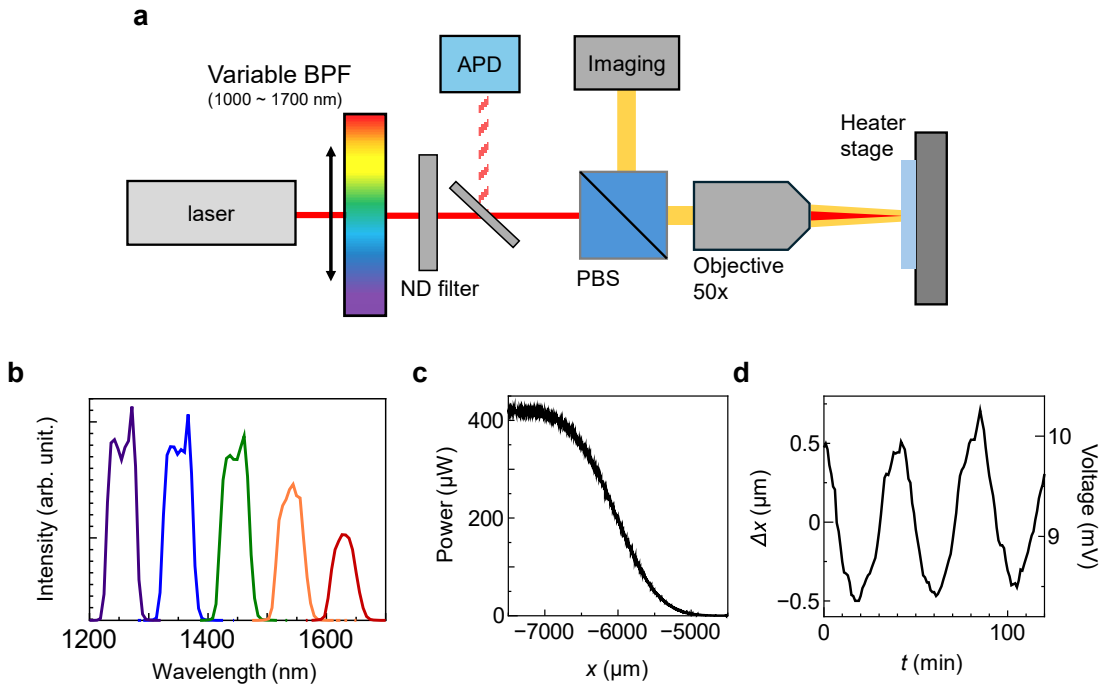

Fig. S2 (a) Schematic of the experiment setup of trench spectroscopy. (b) Transmission spectra of laser beam after the variable band-pass filter. (c) Position of the knife-edge placed in front of the objective lens and the corresponding reflected light intensity from the sample.

Light emitted from a white laser source (SuperK COMPACT, NKT Photonics) passes through a variable band-pass filter and a polarized beam splitter (PBS) and is then focused onto the sample by a 50× objective lens (M Plan Apo NIR 50x, Mitutoyo). The sample was mounted on a three-axis stage equipped with a heater (Fig. S2a). The variable band-pass filter (BPF) was constructed by combining a long-pass filter (FELHV2, Thorlabs, Inc.) and a short-pass filter (FESHV2, Thorlabs, Inc.) with adjustable spectral overlap (Fig. S2b). The center wavelength of irradiation was continuously tunable from 1100 to 1700 nm and the irradiation wavelength was controlled by mounting this BPF on a linear stage. The laser spot diameter was measured using the knife-edge method. A blocking blade (knife-edge) placed in front of the objective lens was moved by the stage, and the laser power was measured by power sensor placed next to the objective as a function of blade position (Fig. S2c). The intensity profile was fitted with an error function, from which the diameter of the focused laser spot was determined to be 3.3 μm.

The magnitude of the mechanical drift of the sample stage was evaluated by monitoring the reflected light intensity from the sample over several hours (Fig. S2d). The stage drift was found to be less than 1 μm with a period of approximately 40 min.

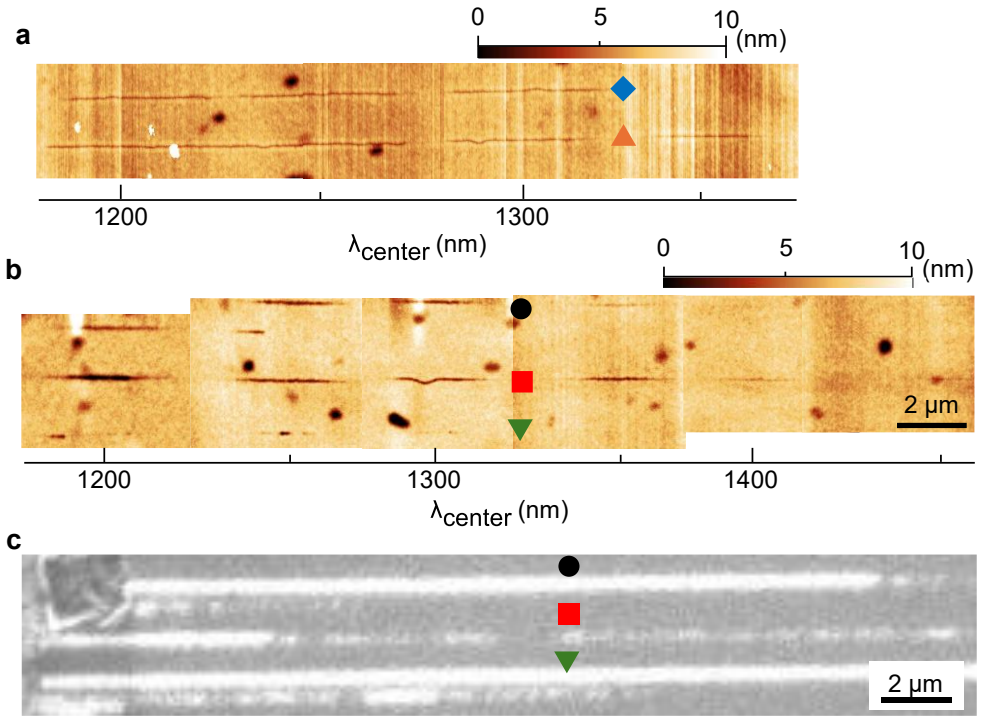

Fig. S3 (a, b) AFM images obtained in trench spectroscopy measurements performed on multiple CNTs. The images are composites assembled from several scans. (c) SEM image of the corresponding CNTs in the same area as shown in (b).

Multiple trenches formed under different irradiation conditions are observed along long, horizontally aligned CNTs. The corresponding trench areas after calibrating the laser power, assuming a linear response are shown in Fig.3a. For the CNTs indicated by the black circle and the green inverted triangle, the SEM contrast suggests that they are metallic CNTs [4]. Such metallic CNTs are expected to exhibit Drude-like absorption that is nearly constant over the investigated wavelength range. Therefore, the wavelength-dependent attenuation observed in Fig. 3a for these CNTs may primarily reflect the trench formation responsivity, which is shown in Fig. 4h.

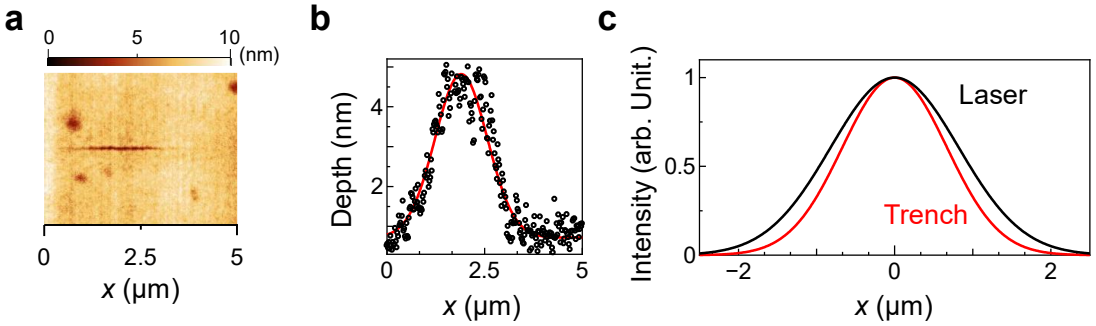

Fig. S4 (a) AFM topography image of a representative trench. (b) Corresponding trench depth profile along the CNT axis and its Gaussian fitting. (c) Comparison between the laser intensity profile and the Gaussian profile derived from the trench depth.

The nonlinear effect of laser-induced thermocapillary flow was analyzed from the viewpoint of the formed trench morphology. If the trench depth were to reflect the irradiation laser power linearly, the axial trench profile along the CNT would be expected to be broadened compared to the laser intensity profile due to axial heat conduction and mechanical drift of the sample stage. However, for the trench shown in Fig. S4a, the axial trench profile was well fitted by a Gaussian function, as shown in Fig. S4b, yielding a standard deviation of $\sigma_{\mathrm{trench}} = 0.67$ μm. Assuming an ideal Gaussian beam, the laser spot size of 3.3 μm corresponds to $\sigma_{\mathrm{laser}} \approx 0.82$ μm, which is larger than the σ obtained from the trench profile. This result indicates that trench formation does not linearly follow the laser intensity distribution and supports the presence of a threshold-like nonlinear response in laser-induced thermocapillary flow.

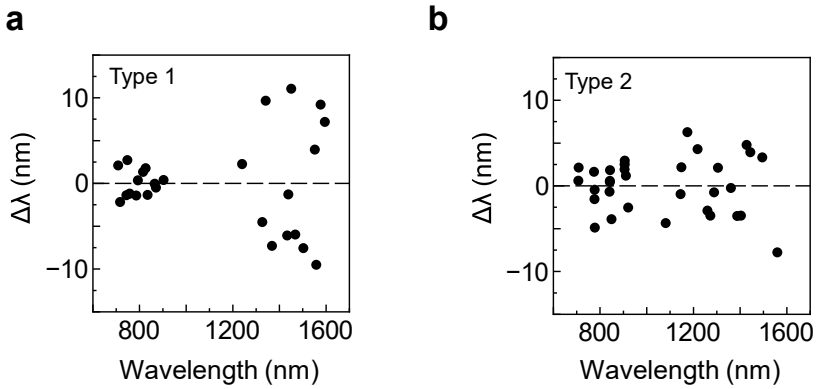

Fig. S5 (a,b) Deviation between the experimentally reported E_{11} and E_{22} wavelengths and the phenomenological model for type 1 CNTs (a) and for type 2 CNTs (b).

The excitonic transition energies E_{11} and E_{22} of the (23,7) CNT were estimated by applying a phenomenological formula that reproduces the photoluminescence excitation (PLE) data reported by Ishii *et al.* [5], in which air-suspended CNTs were wrapped with molecules from atmosphere, presumably water molecules. In this approach, CNT chirality (*n*,*m*) was classified into two groups: type 1 for $n - m \equiv 1 \pmod 3$ and type 2 for $n - m \equiv 2 \pmod 3$. Independent expressions were constructed for the E_{11} and E_{22} transition wavelength λ_{ii} of each type. We assume

$$\lambda_{ii} = \frac{\lambda_{ii}^{*} + \alpha_{ii}^{\nu} \cos(3\theta) + \beta_{ii}^{\nu}}{\gamma_{ii}^{\nu}},$$

where θ is the chiral angle and the λ_{ii}^{*} is transition wavelengths calculated within a nearest-neighbor tight-binding model, α_{ii}^{ν}, β_{ii}^{ν}, and γ_{ii}^{ν} are independent fitting parameters for E_{ii} transition of type-ν CNTs. Using these expressions, the deviation $\Delta\lambda$ between this phenomenological model and the experimental E_{ii} peak wavelengths reported in the PLE measurements [5] was evaluated. The deviation $\Delta\lambda$ is summarized in Fig. S5 for type 1 and type 2. We then estimate the absorption peak wavelengths of the (23,7) CNT by extrapolating the model. Considering the ambiguity in assigning the chirality of thick CNTs by RBM, Kataura plot, and G-band line shape, we should also compare the measured spectrum and estimated spectra for (22,9) and (24,5) CNTs, which suggest the redshift of excitonic response being 18 and 48 meV, respectively.

Reference

[1] J. Song, C. Lu, C. Zhang, S. H. Jin, Y. Li, S. N. Dunham, X. Xie, F. Du, Y. Huang, and J. A. Rogers, "Modeling of thermocapillary flow to purify single-walled carbon nanotubes," *RSC Adv.* **4**, 42454 (2014).

[2] F. Sidorov and A. Rogozhin, "Thermal Reflow Simulation for PMMA Structures with Nonuniform Viscosity Profile," *Polymers* **15**, 3731 (2023).

[3] R. Saito, A. Jorio, J. H. Hafner, C. M. Lieber, M. Hunter, T. McClure, G. Dresselhaus, and M. S. Dresselhaus, "Chirality-dependent G-band Raman intensity of carbon nanotubes," *Phys. Rev. B* **64**, 853121 (2001).

[4] Y. He, J. Zhang, D. Li, J. Wang, Q. Wu, Y. Wei, L. Zhang, J. Wang, P. Liu, Q. Li, S. Fan, and K. Jiang, "Evaluating Bandgap Distributions of Carbon Nanotubes via Scanning Electron Microscopy Imaging of the Schottky Barriers," *Nano Lett.* **13**, 5556 (2013).

[5] A. Ishii, M. Yoshida, and Y. K. Kato, "Exciton diffusion, end quenching, and exciton-exciton annihilation in individual air-suspended carbon nanotubes," *Phys. Rev. B* **91**, 125427 (2015).